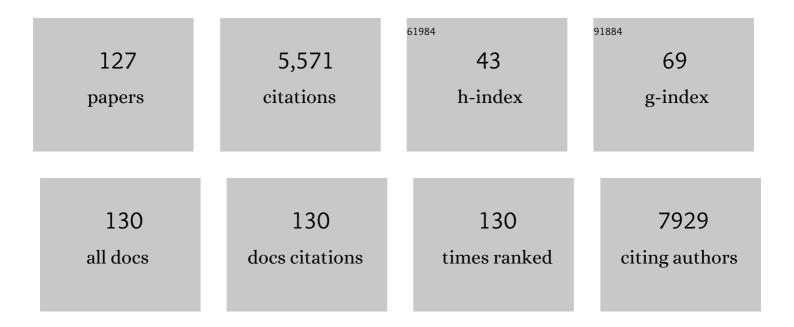
Martin D De Jonge

List of Publications by Year in descending order

Source: https://exaly.com/author-pdf/1307978/publications.pdf Version: 2024-02-01



#	Article	IF	CITATIONS
1	High-speed free-run ptychography at the Australian Synchrotron. Journal of Synchrotron Radiation, 2022, 29, 480-487.	2.4	6
2	Multimodal synchrotron X-ray fluorescence imaging reveals elemental distribution in seeds and seedlings of the Zn–Cd–Ni hyperaccumulator <i>Noccaea caerulescens</i> . Metallomics, 2022, 14, .	2.4	5
3	Synchrotron-Based X-Ray Fluorescence Microscopy Reveals Accumulation of Polymyxins in Single Human Alveolar Epithelial Cells. Antimicrobial Agents and Chemotherapy, 2021, 65, .	3.2	5
4	High-accuracy mass attenuation coefficients and X-ray absorption spectroscopy of zinc – the first X-ray Extended Range Technique-like experiment in Australia. Journal of Synchrotron Radiation, 2021, 28, 1476-1491.	2.4	2
5	High-accuracy measurement of mass attenuation coefficients and the imaginary component of the atomic form factor of zinc from 8.51â€keV to 11.59â€keV, and X-ray absorption fine structure with investigation of zinc theory and nanostructure. Journal of Synchrotron Radiation, 2021, 28, 1492-1503.	2.4	1
6	Manganese accumulation in probiotic Lactobacillus paracasei ATCC 55544 analyzed by synchrotron X-ray fluorescence microscopy and impact of accumulation on the bacterial viability following encapsulation. Food Research International, 2021, 147, 110528.	6.2	2
7	"A spectroscopic picture paints 1000 words―mapping iron speciation in brain tissue with "full spectrum per pixel―X-ray absorption near-edge structure spectroscopy. Clinical Spectroscopy, 2021, 3, 100017.	1.3	4
8	X-ray fluorescence elemental mapping of roots, stems and leaves of the nickel hyperaccumulators Rinorea cf. bengalensis and Rinorea cf. javanica (Violaceae) from Sabah (Malaysia), Borneo. Plant and Soil, 2020, 448, 15-36.	3.7	11
9	Confocal Volumetric μXRF and Fluorescence Computed μ-Tomography Reveals Arsenic Three-Dimensional Distribution within Intact <i>Pteris vittata</i> Fronds. Environmental Science & Technology, 2020, 54, 745-757.	10.0	19
10	The XFM beamline at the Australian Synchrotron. Journal of Synchrotron Radiation, 2020, 27, 1447-1458.	2.4	75
11	Revealing differences in the chemical form of zinc in brain tissue using K-edge X-ray absorption near-edge structure spectroscopy. Metallomics, 2020, 12, 2134-2144.	2.4	8
12	Revealing the Elemental Distribution within Latent Fingermarks Using Synchrotron Sourced X-ray Fluorescence Microscopy. Analytical Chemistry, 2019, 91, 10622-10630.	6.5	22
13	Simultaneous nanostructure and chemical imaging of intact whole nematodes. Chemical Communications, 2019, 55, 1052-1055.	4.1	9
14	Absorption of foliar-applied Zn in sunflower (<i>Helianthus annuus</i>): importance of the cuticle, stomata and trichomes. Annals of Botany, 2019, 123, 57-68.	2.9	81
15	Monitoring compositional changes in Ni(OH) ₂ electrocatalysts employed in the oxygen evolution reaction. Analyst, The, 2019, 144, 7318-7325.	3.5	20
16	<i>In situ</i> analyses of inorganic nutrient distribution in sweetcorn and maize kernels using synchrotron-based X-ray fluorescence microscopy. Annals of Botany, 2019, 123, 543-556.	2.9	24
17	Simultaneous X-ray diffraction, crystallography and fluorescence mapping using the Maia detector. Acta Materialia, 2018, 144, 1-10.	7.9	12
18	Xâ€ray elemental mapping techniques for elucidating the ecophysiology of hyperaccumulator plants. New Phytologist, 2018, 218, 432-452.	7.3	104

#	Article	IF	CITATIONS
19	High-Pressure Synthesis, Structural, and Spectroscopic Studies of the Ni–U–O System. Inorganic Chemistry, 2018, 57, 13847-13858.	4.0	14
20	Simultaneous hyperaccumulation of nickel and cobalt in the tree Glochidion cf. sericeum (Phyllanthaceae): elemental distribution and chemical speciation. Scientific Reports, 2018, 8, 9683.	3.3	42
21	Localized zinc distribution in shark vertebrae suggests differential deposition during ontogeny and across vertebral structures. PLoS ONE, 2018, 13, e0190927.	2.5	12
22	The Topobiology of Chemical Elements in Seabird Feathers. Scientific Reports, 2017, 7, 1998.	3.3	8
23	Iron, Copper, and Zinc Concentration in Aβ Plaques in the APP/PS1 Mouse Model of Alzheimer's Disease Correlates with Metal Levels in the Surrounding Neuropil. ACS Chemical Neuroscience, 2017, 8, 629-637.	3.5	107
24	Polycrystalline materials analysis using the Maia pixelated energy-dispersive X-ray area detector. Powder Diffraction, 2017, 32, S16-S21.	0.2	4
25	Radiation Dose Limits for Bioanalytical X-ray Fluorescence Microscopy. Analytical Chemistry, 2017, 89, 12168-12175.	6.5	45
26	Favored local structures in amorphous colloidal packings measured by microbeam X-ray diffraction. Proceedings of the National Academy of Sciences of the United States of America, 2017, 114, 10344-10349.	7.1	16
27	Spiral scanning X-ray fluorescence computed tomography. Optics Express, 2017, 25, 23424.	3.4	28
28	Strontium mineralization of shark vertebrae. Scientific Reports, 2016, 6, 29698.	3.3	18
29	Novel application of X-ray fluorescence microscopy (XFM) for the non-destructive micro-elemental analysis of natural mineral pigments on Aboriginal Australian objects. Analyst, The, 2016, 141, 3657-3667.	3.5	13
30	A library of AuNPs modified by RAFT polymers of different charge and chain length: high throughput synthesis and synchrotron XFM imaging using a zebrafish larvae model. RSC Advances, 2016, 6, 23550-23563.	3.6	6
31	X-ray fluorescence microscopic measurement of elemental distribution in the mouse retina with age. Metallomics, 2016, 8, 1110-1121.	2.4	5
32	Simultaneous X-ray fluorescence and scanning X-ray diffraction microscopy at the Australian Synchrotron XFM beamline. Journal of Synchrotron Radiation, 2016, 23, 1151-1157.	2.4	19
33	Ferric minerals and organic matter change arsenic speciation in copper mine tailings. Environmental Pollution, 2016, 218, 835-843.	7.5	25
34	A Hidden Portrait by Edgar Degas. Scientific Reports, 2016, 6, 29594.	3.3	61
35	Calculation of Projected Bond-Orientational Order Parameters to Quantify Local Symmetries from Transmission Diffraction Data. Physical Review Letters, 2016, 116, 205501.	7.8	13
36	φXANES: In vivo imaging of metal-protein coordination environments. Scientific Reports, 2016, 6, 20350.	3.3	37

#	Article	IF	CITATIONS
37	High-resolution complementary chemical imaging of bio-elements in <i>Caenorhabditis elegans</i> . Metallomics, 2016, 8, 156-160.	2.4	22
38	Direct in vivo imaging of ferrous iron dyshomeostasis in ageing Caenorhabditis elegans. Chemical Science, 2015, 6, 2952-2962.	7.4	86
39	Mechanisms of murine cerebral malaria: Multimodal imaging of altered cerebral metabolism and protein oxidation at hemorrhage sites. Science Advances, 2015, 1, e1500911.	10.3	25
40	Significant Accumulation of Polymyxin in Single Renal Tubular Cells: A Medicinal Chemistry and Triple Correlative Microscopy Approach. Analytical Chemistry, 2015, 87, 1590-1595.	6.5	54
41	Validation of aGeant4model of the X-ray fluorescence microprobe at the Australian Synchrotron. Journal of Synchrotron Radiation, 2015, 22, 354-365.	2.4	5
42	Microelemental characterisation of Aboriginal Australian natural Fe oxide pigments. Analytical Methods, 2015, 7, 7363-7380.	2.7	8
43	Imaging metals in biology: balancing sensitivity, selectivity and spatial resolution. Chemical Society Reviews, 2015, 44, 5941-5958.	38.1	154
44	X-ray fluorescence microscopy of zinc localization in wheat grains biofortified through foliar zinc applications at different growth stages under field conditions. Plant and Soil, 2015, 392, 357-370.	3.7	50
45	Elemental mapping of the entire intact Drosophila gastrointestinal tract. Journal of Biological Inorganic Chemistry, 2015, 20, 979-987.	2.6	28
46	An investigation into the interactions of gold nanoparticles and anti-arthritic drugs with macrophages, and their reactivity towards thioredoxin reductase. Journal of Inorganic Biochemistry, 2015, 142, 28-38.	3.5	42
47	Characterization of an indirect X-ray imaging detector by simulation and experiment. Ultramicroscopy, 2015, 148, 20-24.	1.9	5
48	Palaeomagnetic and synchrotron analysis of >1.95 Ma fossil-bearing palaeokarst at Haasgat, South Africa. South African Journal of Science, 2014, 110, 1-12.	0.7	14
49	Speciation mapping of environmental samples using XANES imaging. Environmental Chemistry, 2014, 11, 341.	1.5	55
50	Synthesis and Biological Evaluation of a Class of Mitochondriallyâ€Targeted Gadolinium(III) Agents. Chemistry - A European Journal, 2014, 20, 16602-16612.	3.3	22
51	Mapping iron in human heart tissue with synchrotron x-ray fluorescence microscopy and cardiovascular magnetic resonance. Journal of Cardiovascular Magnetic Resonance, 2014, 16, 80.	3.3	24
52	Laterally resolved speciation of arsenic in roots of wheat and rice using fluorescenceâ€ <scp>XANES</scp> imaging. New Phytologist, 2014, 201, 1251-1262.	7.3	81
53	Quantitative synchrotron X-ray fluorescence study of the penetration of transferrin-conjugated gold nanoparticles inside model tumour tissues. Nanoscale, 2014, 6, 9774-9782.	5.6	30
54	High mitochondrial accumulation of new gadolinium(<scp>iii</scp>) agents within tumour cells. Chemical Communications, 2014, 50, 2252-2254.	4.1	31

#	Article	IF	CITATIONS
55	Quantitation and localization of intracellular redox active metals by X-ray fluorescence microscopy in cortical neurons derived from APP and APLP2 knockout tissue. Metallomics, 2014, 6, 1894-1904.	2.4	21
56	X-ray fluorescence imaging reveals subcellular biometal disturbances in a childhood neurodegenerative disorder. Chemical Science, 2014, 5, 2503-2516.	7.4	38
57	Localization of iron in rice grain using synchrotron X-ray fluorescence microscopy and high resolution secondary ion mass spectrometry. Journal of Cereal Science, 2014, 59, 173-180.	3.7	65
58	Copper and lactational hormones influence the CTR1 copper transporter in PMC42-LA mammary epithelial cell culture models. Journal of Nutritional Biochemistry, 2014, 25, 377-387.	4.2	14
59	X-ray nanoprobes and diffraction-limited storage rings: opportunities and challenges of fluorescence tomography of biological specimens. Journal of Synchrotron Radiation, 2014, 21, 1031-1047.	2.4	61
60	Systematic Mapping of Icosahedral Short-Range Order in a Melt-Spun <mml:math xmlns:mml="http://www.w3.org/1998/Math/MathML" display="inline"><mml:msub><mml:mi>Zr</mml:mi><mml:mn>36</mml:mn></mml:msub><mml:msub><mml:m Glass. Physical Review Letters, 2013, 110, 205505.</mml:m </mml:msub></mml:math 	ıi>℃ů <td>nl:mi><mml:n< td=""></mml:n<></td>	nl:mi> <mml:n< td=""></mml:n<>
61	Can biological toxicity drive the contrasting behavior of platinum and gold in surface environments?. Chemical Geology, 2013, 343, 99-110.	3.3	40
62	Quantification of ZnO Nanoparticle Uptake, Distribution, and Dissolution within Individual Human Macrophages. ACS Nano, 2013, 7, 10621-10635.	14.6	116
63	Secondary vitellogenesis persists despite disrupted fecundity in amphipods maintained on metal-contaminated sediment: X-ray fluorescence assessment of oocyte metal content. Ecotoxicology and Environmental Safety, 2013, 93, 31-38.	6.0	3
64	Relating Cytotoxicity, Zinc Ions, and Reactive Oxygen in ZnO Nanoparticle–Exposed Human Immune Cells. Toxicological Sciences, 2013, 136, 120-130.	3.1	198
65	Distribution and speciation of Mn in hydrated roots of cowpea at levels inhibiting root growth. Physiologia Plantarum, 2013, 147, 453-464.	5.2	21
66	Direct in vivo imaging of essential bioinorganics in Caenorhabditis elegans. Metallomics, 2013, 5, 627.	2.4	40
67	Quantitative mapping of the oxidative effects of mantle metasomatism. Geology, 2013, 41, 683-686.	4.4	20
68	Quantitative determination of metal and metalloid spatial distribution in hydrated and fresh roots of cowpea using synchrotron-based X-ray fluorescence microscopy. Science of the Total Environment, 2013, 463-464, 131-139.	8.0	38
69	In Situ Speciation and Distribution of Toxic Selenium in Hydrated Roots of Cowpea. Plant Physiology, 2013, 163, 407-418.	4.8	18
70	Mapping Element Distributions in Plant Tissues Using Synchrotron X-ray Fluorescence Techniques. Methods in Molecular Biology, 2013, 953, 143-159.	0.9	10
71	Iron-rich particles in heavily contaminated multicrystalline silicon wafers and their response to phosphorus gettering. Semiconductor Science and Technology, 2012, 27, 125016.	2.0	12
72	Caenorhabditis elegans Maintains Highly Compartmentalized Cellular Distribution of Metals and Steep Concentration Gradients of Manganese. PLoS ONE, 2012, 7, e32685.	2.5	47

#	Article	IF	CITATIONS
73	Examination of the Distribution of Arsenic in Hydrated and Fresh Cowpea Roots Using Two- and Three-Dimensional Techniques Â. Plant Physiology, 2012, 159, 1149-1158.	4.8	43
74	A review of recent developments in the speciation and location of arsenic and selenium in rice grain. Analytical and Bioanalytical Chemistry, 2012, 402, 3275-3286.	3.7	79
75	Getting to the core of platinum drug bio-distributions: the penetration of anti-cancer platinum complexes into spheroid tumour models. Metallomics, 2012, 4, 1209.	2.4	56
76	Antagonism between transition metal pro-oxidants in polyethylene films. Polymer Degradation and Stability, 2012, 97, 1178-1188.	5.8	21
77	Systematic functional characterization of putative zinc transport genes and identification of zinc toxicosis phenotypes in <i>Drosophila melanogaster</i> . Journal of Experimental Biology, 2012, 215, 3254-65.	1.7	48
78	Fate of Intravenously Administered Gold Nanoparticles in Hair Follicles: Follicular Delivery, Pharmacokinetic Interpretation, and Excretion. Advanced Healthcare Materials, 2012, 1, 736-741.	7.6	19
79	A step toward standardization: development of accurate measurements of X-ray absorption and fluorescence. Journal of Synchrotron Radiation, 2012, 19, 851-862.	2.4	12
80	Losses of essential mineral nutrients by polishing of rice differ among genotypes due to contrasting grain hardness and mineral distribution. Journal of Cereal Science, 2012, 56, 307-315.	3.7	59
81	The use of spectroscopic imaging and mapping techniques in the characterisation and study of DLD-1 cell spheroid tumour models. Integrative Biology (United Kingdom), 2012, 4, 1072-1080.	1.3	32
82	High-Definition X-ray Fluorescence Elemental Mapping of Paintings. Analytical Chemistry, 2012, 84, 3278-3286.	6.5	79
83	Determination of the oxidation state of Cu in substituted Cu-In-Fe-bearing sphalerite via Â-XANES spectroscopy. American Mineralogist, 2012, 97, 476-479.	1.9	114
84	Human Amnion Epithelial Cells Induced to Express Functional Cystic Fibrosis Transmembrane Conductance Regulator. PLoS ONE, 2012, 7, e46533.	2.5	23
85	Megapixel imaging of (micro)nutrients in mature barley grains. Journal of Experimental Botany, 2011, 62, 273-282.	4.8	134
86	Uptake, Distribution, and Speciation of Selenoamino Acids by Human Cancer Cells: X-ray Absorption and Fluorescence Methods. Biochemistry, 2011, 50, 1641-1650.	2.5	50
87	Metabolism of Selenite in Human Lung Cancer Cells: X-Ray Absorption and Fluorescence Studies. Journal of the American Chemical Society, 2011, 133, 18272-18279.	13.7	73
88	X-ray Absorption and Micro X-ray Fluorescence Spectroscopy Investigation of Copper and Zinc Speciation in Biosolids. Environmental Science & Technology, 2011, 45, 7249-7257.	10.0	75
89	Distribution of Metals in the Termite Tumulitermes tumuli (Froggatt): Two Types of Malpighian Tubule Concretion Host Zn and Ca Mutually Exclusively. PLoS ONE, 2011, 6, e27578.	2.5	37
90	Examination of trafficking of phagocytosed colloid particles in neutrophils using synchrotron-based X-ray fluorescence microscopy (XFM). Journal of Biological Physics, 2011, 37, 493-506.	1.5	1

#	Article	IF	CITATIONS
91	Trends in hard X-ray fluorescence mapping: environmental applications in the age of fast detectors. Analytical and Bioanalytical Chemistry, 2011, 400, 1637-1644.	3.7	93
92	Quantitative comparison of preparation methodologies for x-ray fluorescence microscopy of brain tissue. Analytical and Bioanalytical Chemistry, 2011, 401, 853-864.	3.7	53
93	Measuring the linearity of X-ray detectors: consequences for absolute attenuation, scattering and absolute Bragg intensities. Journal of Applied Crystallography, 2011, 44, 281-286.	4.5	10
94	Phosphorus <i>K</i> -edge XANES spectroscopy of mineral standards. Journal of Synchrotron Radiation, 2011, 18, 189-197.	2.4	130
95	In Situ Distribution and Speciation of Toxic Copper, Nickel, and Zinc in Hydrated Roots of Cowpea Â. Plant Physiology, 2011, 156, 663-673.	4.8	130
96	Fast X-Ray Fluorescence Microtomography of Hydrated Biological Samples. PLoS ONE, 2011, 6, e20626.	2.5	89
97	Detection of Genetically Altered Copper Levels in Drosophila Tissues by Synchrotron X-Ray Fluorescence Microscopy. PLoS ONE, 2011, 6, e26867.	2.5	18
98	Energy determination of synchrotron X-ray beam energy in the high energy region of 38–50keV using powder diffraction patterns of the standard powder Si640b. Nuclear Instruments and Methods in Physics Research, Section A: Accelerators, Spectrometers, Detectors and Associated Equipment, 2010, 619, 147-149.	1.6	4
99	An energy and intensity monitor for X-ray absorption near-edge structure measurements. Nuclear Instruments and Methods in Physics Research, Section A: Accelerators, Spectrometers, Detectors and Associated Equipment, 2010, 619, 154-156.	1.6	5
100	Scanning Xâ€ray fluorescence microspectroscopy of metallic impurities in solarâ€grade silicon. Physica Status Solidi (A) Applications and Materials Science, 2010, 207, 1807-1810.	1.8	8
101	Quantitative 3D elemental microtomography of <i>Cyclotella meneghiniana</i> at 400-nm resolution. Proceedings of the National Academy of Sciences of the United States of America, 2010, 107, 15676-15680.	7.1	146
102	X-ray mass attenuation coefficients and imaginary components of the atomic form factor of zinc over the energy range of 7.2–15.2 keV. Physical Review A, 2010, 81, .	2.5	24
103	Hard X-ray fluorescence tomography—an emerging tool for structural visualization. Current Opinion in Structural Biology, 2010, 20, 606-614.	5.7	153
104	Reduced As components in highly oxidized environments: Evidence from full spectral XANES imaging using the Maia massively parallel detector. American Mineralogist, 2010, 95, 884-887.	1.9	52
105	Nano-roughness in gold revealed from X-ray signature. Physics Letters, Section A: General, Atomic and Solid State Physics, 2009, 373, 1177-1180.	2.1	15
106	Anoxic versus oxic sample pretreatment: Effects on the speciation of sulfur and iron in well-aerated and wetland soils as assessed by X-ray absorption near-edge spectroscopy (XANES). Geoderma, 2009, 153, 318-330.	5.1	29
107	Characterization of phosphorus, calcium, iron, and other elements in organisms at subâ€micron resolution using Xâ€ray fluorescence spectromicroscopy. Limnology and Oceanography: Methods, 2009, 7, 42-51.	2.0	23
108	Differential phase contrast with a segmented detector in a scanning X-ray microprobe. Journal of Synchrotron Radiation, 2008, 15, 355-362.	2.4	75

#	Article	IF	CITATIONS
109	Highâ€resolution Xâ€ray imaging of <i>Plasmodium falciparum</i> â€infected red blood cells. Cytometry Part A: the Journal of the International Society for Analytical Cytology, 2008, 73A, 949-957.	1.5	49
110	Quantitative Phase Imaging with a Scanning Transmission X-Ray Microscope. Physical Review Letters, 2008, 100, 163902.	7.8	93
111	Exploring Ocean Biogeochemistry by Singleâ€Cell Microprobe Analysis of Protist Elemental Composition ¹ . Journal of Eukaryotic Microbiology, 2008, 55, 151-162.	1.7	34
112	Keyhole coherent diffractive imaging. Nature Physics, 2008, 4, 394-398.	16.7	289
113	Quantitative phase measurement in coherent diffraction imaging. Optics Express, 2008, 16, 3342.	3.4	21
114	Marine Polyphosphate: A Key Player in Geologic Phosphorus Sequestration. Science, 2008, 320, 652-655.	12.6	260
115	Nanoscale Imaging of Buried Structures with Elemental Specificity Using Resonant X-Ray Diffraction Microscopy. Physical Review Letters, 2008, 100, 025504.	7.8	81
116	Measurement of the x-ray mass attenuation coefficient and determination of the imaginary component of the atomic form factor of tin over the energy range of29–60keV. Physical Review A, 2007, 75, .	2.5	42
117	Experimental Measurement of the Four-Dimensional Coherence Function for an Undulator X-Ray Source. Physical Review Letters, 2007, 98, 224801.	7.8	36
118	A method for phase reconstruction from measurements obtained using a configured detector with a scanning transmission X-ray microscope. Nuclear Instruments and Methods in Physics Research, Section A: Accelerators, Spectrometers, Detectors and Associated Equipment, 2007, 582, 218-220.	1.6	8
119	Curved beam coherent diffractive imaging. Thin Solid Films, 2007, 515, 5553-5556.	1.8	9
120	Crystal optics as guard apertures for coherent x-ray diffraction imaging. Optics Letters, 2006, 31, 3194.	3.3	4
121	Improved techniques for measuring x-ray mass attenuation coefficients. Optical Engineering, 2006, 45, 046501.	1.0	7
122	The correction of systematic image deformations inherent to two-dimensional proportional counters. Measurement Science and Technology, 2005, 16, 2280-2286.	2.6	8
123	Measurement of the x-ray mass attenuation coefficient and determination of the imaginary component of the atomic form factor of molybdenum over the13.5–41.5â^'keVenergy range. Physical Review A, 2005, 71, .	2.5	52
124	Full-foil x-ray mapping of integrated column density applied to the absolute determination of mass attenuation coefficients. Measurement Science and Technology, 2004, 15, 1811-1822.	2.6	23
125	X-ray bandwidth: Determination by on-edge absorption and effect on various absorption experiments. Physical Review A, 2004, 69, .	2.5	21
126	Accurate determination of the thickness or mass per unit area of thin foils and single-crystal wafers for x-ray attenuation measurements. Review of Scientific Instruments, 2004, 75, 2943-2949.	1.3	16

#	Article	IF	CITATIONS
127	Absolute determination of the effect of scattering and fluorescence on x-ray attenuation measurements. Journal of Physics B: Atomic, Molecular and Optical Physics, 2004, 37, 3163-3176.	1.5	29